Draft version February 25, 2019
Typeset using LaTeX **preprint** style in AASTeX62

Galactic Interstellar Emission Model for the 4FGL Catalog Analysis

The *Fermi*-LAT collaboration

ABSTRACT

This note documents the development of the Galactic interstellar emission model used for the fourth *Fermi* Large Area Telescope source catalog (4FGL) analysis, `gll_iem_v07.fits`. The model is based on an analysis of the first 8 years of LAT data (Pass 8 P8_R3) and benefits from a variety of multiwavelength tracers of the interstellar medium, and improved derivation of other components.

1. INTRODUCTION

The sky in high-energy (>50 MeV) γ rays is dominated by emission from interstellar processes in the Milky Way. The space between the stars is threaded by cosmic rays (CRs) that propagate throughout (and are largely confined to) the Milky Way. Interactions of CR protons with interstellar nuclei produce γ rays through decay of secondary pions. Interactions of CR electrons with nucleons produce γ rays via Bremsstrahlung and inverse Compton scattering of CR electrons with low-energy (infrared-ultraviolet) photons of the interstellar radiation field (ISRF) also produce γ rays. The column densities of interstellar gas and intensity of the ISRF are low enough that once produced, the γ rays with energies below several hundred GeV typically undergo no further interaction in crossing the Milky Way. The resulting emission observed at Earth is brightest at low Galactic latitudes, and is highly structured, largely reflecting spatial structure of the interstellar gas, although on larger scales variations in the density of CRs and the ISRF also affect the observed intensity. This interstellar γ-ray emission is the background against which discrete γ-ray sources must be detected and characterized.

On consideration of the relatively low counting statistics for γ-ray observations and the limited angular resolution of γ-ray telescopes, an accurate model of the Galactic interstellar emission is desirable. Especially at low Galactic latitudes, otherwise distinguishing between structured interstellar emission and discrete sources can be challenging.

Since the era of COS-B (1975–1982) the interstellar γ-ray emission has been quantitatively modeled using tracers of the interstellar gas, starting with maps of galaxy counts as a measure of interstellar obscuration, a tracer of interstellar dust that is an indirect tracer of interstellar gas (e.g., Lebrun et al. 1982). Models became more sophisticated especially when the first surveys of the CO J=1–0 line, widely used as a tracer of interstellar H_2, became available. Because observations of the CO line (at 2.6 mm) and the H I line (at 21 cm) can measure the emission line profile with typically better than 1 km s^{-1} resolution, the Doppler shifts of the measured spectral lines, together with a model for the overall rotation of the Milky Way, can be used to crudely separate emission along any given line of sight into different ranges of Galactocentric distance (see § 3.1). Because on large scales, the star-formation rate of the Milky Way can be considered to be radially symmetric about the Galactic center (GC), and the remnants of early-type stars are the sources of CRs, on large scales the CR density can be considered to be a function primarily of Galactocentric distance.

Table 1. Pass 8 P8R3 Source class LAT data selection. The Map order column specifies the HEALPix order of the maps. The number of the pixels over the sky is $12 \times 2^{2<\text{order}>}$

Energy range (GeV)	Max. zenith angle (deg)	PSF types	Map order
0.03–0.1	80	3	7
0.1–0.3	90	2, 3	8
0.3–1	100	1, 2, 3	8
1–1000	105	0, 1, 2, 3	9

The ISRF cannot be observed directly, but models of the stellar populations of the Milky Way, and of the interstellar dust that at lower energies redistributes stellar radiation, are detailed and advanced (Porter et al. 2008).

In this note we describe the refinements and updates introduced to the interstellar emission model (IEM) in preparation for the fourth *Fermi* Large Area Telescope (LAT) source catalog (4FGL), which is based on the first 8 years of LAT science data. This is the first major update to the LAT Collaboration's IEM since the model for the 3FGL catalog analysis (referred to here as the 4-year model, Acero et al. 2016). The goal of the development of the new IEM is to improve its accuracy, through use of new multiwavelength survey data and analysis refinements. § 2 describes the data selection, § 3 describes the components of the model, including description of new treatment for the interstellar gas distribution and the interim catalog of LAT γ-ray sources considered during development of the IEM. § 4 describes the fitting procedure used to refine the parameters of the IEM. Finally, § 5 describes the resulting model for interstellar γ-ray emission, including a comparison of the new IEM with the 4-year model. The updates relative to the 4-year model are described in the various subsections.

2. DATA SELECTION

We use the same data selections as for the 4FGL catalog analysis[1], although instead of considering each PSF type/energy range/zenith angle limit selection independently as for the catalog analysis, we combine data sets for different PSF event types within each energy range, to end up with the four data sets described in Table 1. As for the 4FGL catalog, the analysis was based on Pass 8 P8R3 Source class events. Each data set spans the 8-year time interval of the 4FGL catalog analysis and has the same Good Time Interval selections, which exclude time intervals containing bright γ-ray bursts or solar flares, amounting to less than three days. Table 1 also lists the spatial binning (HEALPix map order, Górski et al. 2005) for the different data selections[2]. The map order increases with the energy range, so that the binning is always finer than the width of the effective point-spread function, which narrows with increasing energy up to ∼10 GeV.

[1] See the 4FGL documentation at the *Fermi* Science Support Center, https://fermi.gsfc.nasa.gov/ssc/.
[2] http://healpix.sourceforge.net

3. MODEL DESCRIPTION

The radiative transfer of high-energy γ rays through the Milky Way is trivial, and we model the intensity of the emission of the Milky Way as a linear combination of templates representing various components of the emission as described below.

3.1. *Gas templates: H I and CO*

As noted in § 1, spectral line surveys of H I and CO have long been used to study the distribution of gas across the Milky Way. If the Milky Way is modeled as being in uniform circular rotation with some rotation curve $\Theta(R)$, for some distance $R_\odot$ of the Sun from the GC, the line-of-sight velocity of a spectral line can be uniquely related to the distance of the emitting gas from the GC, and so a spectral line survey can be 'decomposed' into rings of Galactocentric distance.

For the new model we extensively updated the procedure for deriving Galactocentric 'rings' of interstellar H I and H_2. We summarize the updates here; the details will be presented elsewhere (Q. Remy et al., in prep).

- **New H I survey.** To trace the interstellar H I, instead of the Leiden-Argentine-Bonn all-sky survey (Kalberla et al. 2005) we now use the HI4PI all-sky survey (HI4PI Collaboration et al. 2016), which provides better angular resolution (16.2′ vs. 36′) FWHM beamwidth), comparable velocity resolution (1.29 km s^{-1} vs. 1.03 km s^{-1} per channel) and better sensitivity per channel (∼43 mK vs. 80 mK RMS).

- **New rotation curve.** We now use the rotation curve of Sofue (2015) with $R_\odot = 8$ kpc and $\Theta_\odot = 238$ km s^{-1} instead of the rotation curve of Clemens (1985). The differences are not dramatic: the profiles are quite similar for $R < 2$ kpc (bulge region), and differ somewhat more at larger R.

- **New spectral line profile fitting.** Formerly, for a given H I or CO spectrum we assigned gas to rings channel by channel. Now we fit emission line profiles for each spectrum, and assign the entire emission of a given line to the ring that contains the central velocity of the profile. This reduces 'blending' of rings due to the intrinsic velocity dispersions of individual interstellar clouds, although it cannot mitigate blending effects from random or systematic velocities of clouds with respect to uniform circular rotation.

- **New interpolation across the GC and anticenter regions.** In the ∼20 deg of longitude around the Galactic center and anticenter, the line-of-sight velocities due to uniform circular rotation are close to zero and do not provide useful kinematic discrimination. Formerly we used a linear interpolation scheme to make the rings span these important longitude ranges. Now we also consider an analytical model (from GALPROP) for the surface density distribution to guide the interpolation. In any case, the overall column densities of H I or integrated CO line intensities for the spectra are respected in the interpolation.

In addition, we adopted a spin temperature $T_{\rm spin} = 300$ K for the optical depth correction of the HI4PI survey data. This is higher than the 140 K spin temperature adopted for the LAB survey in development of the H I rings for the 4-year model, but at the higher resolution of the HI4PI survey, the brightest regions are much less beam diluted. In any case, the Dark Neutral Medium (DNM) component (§ 3.2) is derived using H I rings with the same $T_{\rm spin}$ and we can expect that the DNM

Table 2. Galactocentric radius ranges for the rings used as templates in the model fitting. Note that we have adopted $R_\odot = 8$ kpc, and ring 6 is the 'local' ring that includes the solar circle.

Ring number	Radius range (kpc)
0	0–0.15
1	0.15–0.6
2	0.6–2
3	2–4
4	4–6
5	6–7
6	7–9
7	9–12
8	12–15
9	15–35

component provides a degree of 'column density correction' for directions for which the adopted $T_{\rm spin}$ is inaccurate.

As for the 4-year model we continue to use the CfA CO survey for CO spectra. It remains the largest uniform survey of the CO J=1-0 line, with $\sim 9'$ FWHM resolution at low latitudes and 1.3 km s^{-1} velocity resolution.

Several considerations relate to selecting the Galactocentric radius ranges for partitioning the H I and CO survey data into rings of N(H I) and $W_{\rm CO}$:

- The number of templates should be as small as reasonably possible, to reduce the number of degrees of freedom in the model and to reduce covariance between the rings;
- The resolution in Galactocentric distance of any decomposition scheme is limited by the approximation of uniform circular motion vs. the reality of streaming motions and random velocity deviations;
- The distribution of CRs is likely to be smooth on kiloparsec scales across the disk (and to have a large scale height vertical to the disk);
- The interstellar gas in the Central Molecular Zone (inner $\sim$150 pc from the GC) is quite different from the rest of the Galaxy (e.g., the CO line widths are extremely broad, effectively decreasing the optical depth of the emission) and the innermost rings are relatively small because the gradient of gas properties is steep.

Table 2 lists the ranges of Galactocentric distance used to define templates for the model fitting.

3.2. *Dark Gas*

The 'dark gas' or dark neutral medium (DNM), is the component of the cold interstellar medium that is not traced in H I or CO emission. Its existence was established by Grenier et al. (2005) based on intercomparison of dust thermal emission maps with H I, CO, and γ-ray observations. For dust emission, they used the Schlegel et al. (1998) map (SFD) of interstellar reddening E(B–V), derived from *IRAS* and *COBE* DIRBE infrared and microwave sky survey data, jointly analyzed to distinguish variations in interstellar dust temperature from variations in dust column density. On the assumption that dust is an approximately proportional tracer of interstellar gas, the SFD map clearly indicated a more extensive interstellar medium than traced by H I or CO emission lines (hence 'dark' gas). The interpretation was that the 'extra' component traced by the dust emission was perhaps indicating regions where H_2 is present but CO is photodissociated. The dust emission, which is quite optically thin, can also 'correct' for estimates of column densities of H I that are underestimated due to self-absorption (colder foreground gas in front of warmer gas). Grenier et al. derived the DNM column density by evaluating the residual after the components of the E(B–V) map correlated with the integrated intensity of CO, $W_{\rm CO}$, and the column density of H I, N(H I), were subtracted, i.e., they evaluated the component that is not linearly correlated with either of the spectral line tracers of interstellar gas. This procedure has been widely followed since.

Although we used a similar procedure to Acero et al. (2016) to derive the DNM component, a substantial improvement was enabled by the availability of *Planck* maps of dust optical depth (Planck Collaboration et al. 2016), which have superior angular resolution, and better accuracy around bright star-forming regions, than the SFD E(B–V) map. We use the 353 GHz dust optical depth map[3]. The derivation of the DNM component involves fitting the optical depth map with linear combinations of the same H I and $W_{\rm CO}$ ring maps as used for the IEM fitting. For the DNM, the fitting procedure (least squares) is iterative, with each iteration being a sequence of three fits: local ring (ring 6), outer Galaxy (rings 7–9), and inner Galaxy (rings 0–5).

Figure 1 illustrates the resulting positive and negative DNM component maps used in the model fitting. We emphasize that we do not consider any physical component to represent a negative column density of interstellar gas. Instead we adopt the negative component as a column density correction map in recognition that no single spin temperature applies to every atomic hydrogen cloud across the Milky Way. Additionally, the evaluation of dust optical depth at low latitudes (within 1–2° of the plane) cannot be precise because typically more than one interstellar cloud will be intercepted by any given line of sight. A mitigating consideration is that the dark gas component is largely the 'edges' of molecular clouds; it is quite important in local, relatively low mass and diffuse molecular clouds, which in a sense are largely edges, but less so in terms of overall mass for the giant molecular clouds in the spiral arms of the inner Galaxy, which dominate the interstellar γ-ray emission at low latitudes.

3.3. *Inverse Compton on the Interstellar Radiation Field*

We use a GALPROP (Porter et al. 2017)[4] model (^{S}L^{Z}6^{R}30^{T}150^{C}2, Ackermann et al. 2012), but for some flexibility in fitting, we sub-divide it into the same set of rings as defined in § 3.1. (Note that GALPROP calculates the IC model for separate frequency ranges of the ISRF; we consider only the

[3] `COM_CompMap_Dust-GNILC-Model-Opacity_2048_R2.01.fits` from the *Planck* Legacy Archive, http://pla.esac.esa.int/pla/.

[4] http://galprop.stanford.edu/

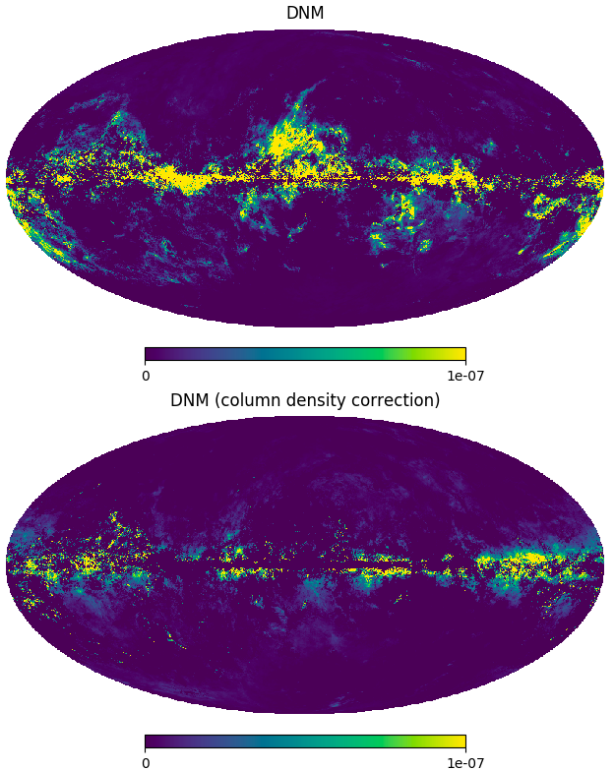

Figure 1. DNM positive (upper) and negative (lower) contributions to the IEM (see text for discussion) illustrated as maps of predicted γ-ray intensity (in cm^{-2} s^{-1} sr^{-1} MeV^{-1}) at 190 MeV. The images have the same, linear, scaling and are in Galactic coordinates in Mollweide projection.

sum of these components.) The freedom in the fit is only individual scale factors for each ring. This does not allow any adjustment of CR electron spectra, but effectively allows for adjustments of the overall intensity of the ISRF and/or CR electron flux as a function of Galactocentric distance.

3.4. *Large-scale structures*

Some components of the Galactic interstellar emission are now well understood not to have multiwavelength counterparts that can be used as templates for modeling the γ-ray emission of the component. Perhaps the best known is the *Fermi* bubbles, large, hard-spectrum 'lobes' extending approximately symmetrically above and below the Galactic equator in the Galactic center region and perhaps related to past activity associated with the massive black hole at the Galactic center (Su et al. 2010). Another is the Galactic center GeV excess, which has a softer spectrum and a smaller angular extent and has been interpreted as being a signal from WIMP dark matter annihilation in the halo of the Milky Way or as a signal from a population of unresolved γ-ray emitting millisecond pulsars in the Galactic bulge (e.g., Hooper & Goodenough 2011; Abazajian & Kaplinghat 2012).

Other components of the interstellar emission may have multiwavelength counterparts, such as the radio continuum emission of the large radio lobe Loop I, but that do not trace the associated γ-ray emission particularly well. Loop I, with an angular extent of $\sim$120°, has been known for decades in the radio, where it is detected in synchrotron emission from high-energy electrons in the magnetic field of the loop. The same general feature is seen in the LAT data, with a fairly soft spectrum. In our development of the new model we explored using the 408 MHz radio continuum map of Haslam et al.

(1982), and an analytical model for the spatial distribution (Wolleben 2007), with unsatisfactory results, and decided to treat the Loop I γ-ray emission as a non-template component, like the *Fermi* bubbles and other non-template residuals.

For components of the interstellar emission that do not have templates in the model, following a procedure similar to that used for the 4-year model, we defined a 'patch' component based on the residual γ-ray intensity from fitting the overall IEM. This was necessarily an iterative process, because the patch component is itself part of the model; the model fitting is described in § 4. For each iteration of the definition of the patch component we used residuals from the previous fit, constrained to be non-negative and spatially smoothed with a 2-dimensional Gaussian of FWHM 3°. The contributions from the patch component were important only in a large region around the Galactic center, encompassing Loop I and the *Fermi* bubbles, and along the Galactic equator in the first and second quadrants, and we applied a mask to limit the spatial extent to the region indicated by the blue outlines in Figure 2. The region of the patch component is substantially the same as for the non-template residual component in the 4-year model Acero et al. (2016).

A refinement to the definition of the patch component was implemented to enforce spectral smoothness in addition to spatial smoothness, and also in recognition of the emission as likely being due to populations of CR electrons (which have relatively limited lifetime and range) with characteristic power-law spectra. With the patch component residuals binned to 11 planes in energy and rebinned to NSIDE=32 ($\sim$3° pixels) resolution spatially, we fit each line of sight with a doubly broken power-law spectrum, with break energies fixed at 150 MeV and 3 GeV, which empirically provided an adequate representation of the residuals. The resulting fit parameters (maps of a normalization factor and the three spectral indices of the doubly broken power law) were then spatially smoothed with a 3° FWHM Gaussian and the final patch component model was generated using these smoothed parameters.

Defined this way, the patch component should be fairly immune to 'over-tuning' to subtract statistical fluctuations, and importantly it cannot absorb spatial structure on scales less than $\sim$4°. We also restricted the patch component to have non-negative intensity, so that it cannot compensate for over-predictions of γ-ray intensity due to other components of the model.

The resulting model for the patch component is compared with the residual γ-ray intensity that it represents in Figure 2. The spatial distribution of the patch component varies significantly with energy. At low energies, the Loop I component is prominent. At intermediate GeV energies, the enhancement at low latitudes in the first and second quadrants is relatively strong and at higher energies, the *Fermi* bubbles component is prominent.

3.5. *Cataloged sources*

The model was developed with a succession of preliminary 4FGL source lists, ending up with the `uw8505` list (not released), which was derived based on a near-final version of the new Galactic IEM. The fitting procedure for the IEM involved optimizing the diffuse components in large regions of the sky ($\sim$2 sr), which typically included a few thousand of the cataloged sources (see § 4). Joint optimization of the parameters of so many sources was impractical, and instead the great majority of the sources were combined into a 'FixedSources' template, based on their spectral parameters and locations in the `uw8505` list (and their spatial templates, for extended sources). These sources were 'fixed' in the sense of their positions and relative fluxes, and in the fitting for the IEM, they were treated as a single template. Because spectral parameters of typical (i.e., not particularly bright)

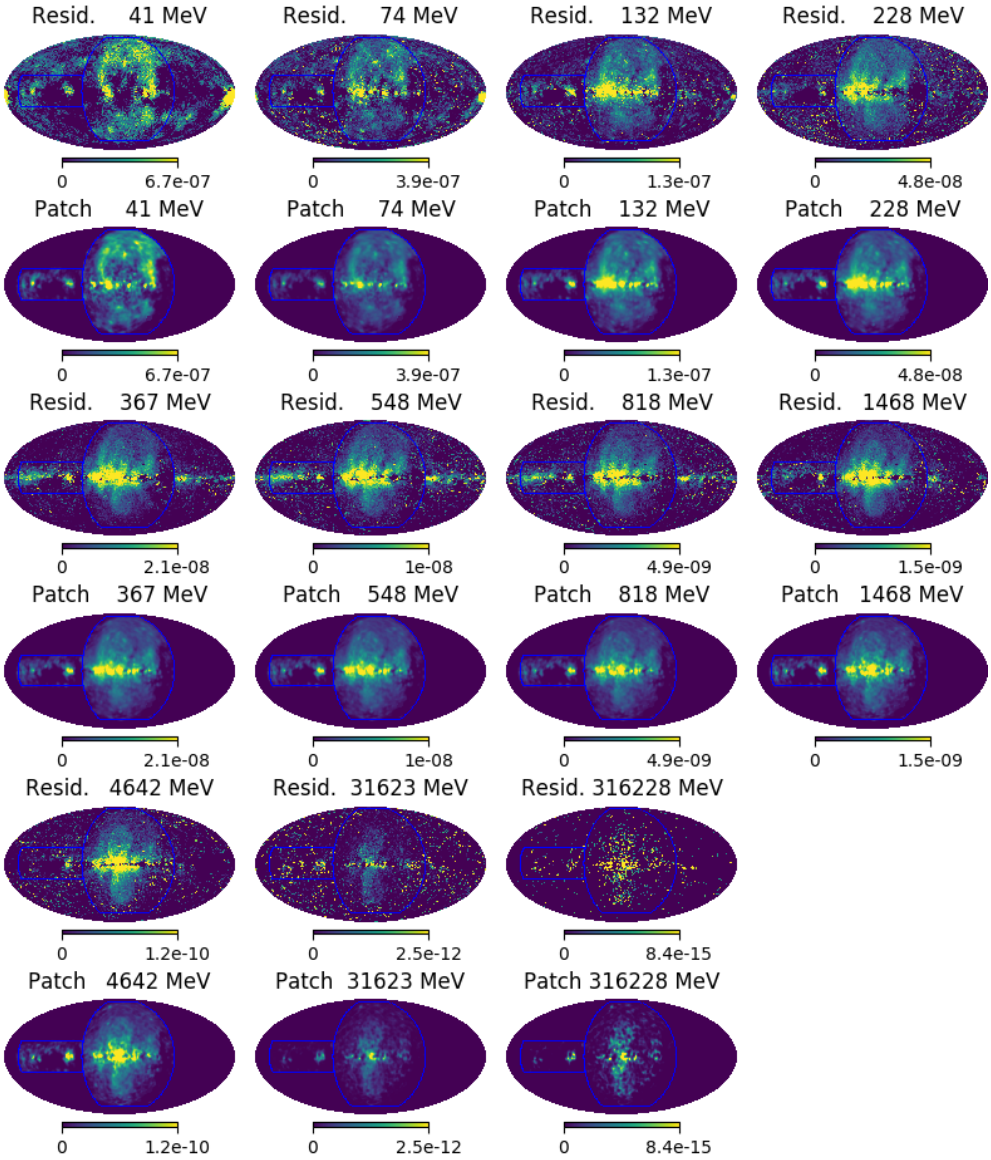

Figure 2. Comparisons between residual γ-ray intensity, in a model fit that has been iterated with a succession of patch components defined to represent the residual intensity, and the final model for the residuals described in the text. The residual intensities and patch model are shown in alternate rows. The maps are in Galactic coordinates in Mollweide projection. The scaling is linear and the intensity units are cm^{-2} s^{-1} sr^{-1} MeV^{-1}. The dark blue outline in the maps of the model components indicate the spatial extent of the patch component.

sources are not particularly well constrained below ∼100 MeV and power-law extrapolations tended to make the FixedSources template too bright at low energies, in developing the FixedSources template we used logParabola spectral parameters for every source, even if in the `uw8505` analysis the source was not found to have a significantly curved spectrum. With these 'best guess' curved spectra, the FixedSources template was much less dominant at low energies. In any case, as noted in § 4, the FixedSources template was always given extensive spectral freedom in the fits.

As a refinement of the procedure, and in recognition that the very brightest discrete sources can locally influence the fit of the IEM, the 100 `uw8505` sources (all-sky) with the greatest energy fluxes in the 0.1–100 GeV range were treated individually in the fits, with each having a free scale factor relative to the `uw8505` spectral model. This is not ideal, in terms of removing potential bias from potential slight spectral mismodeling of the brightest sources, but was a practical compromise in terms of the number of degrees of freedom in the model fits for the large areas of the sky being modeled.

3.6. *Unresolved Galactic sources*

The bright band of interstellar γ-ray emission at low latitudes undoubtedly contains discrete sources that are too faint to be detected individually. Extragalactic unresolved sources are assumed to contribute to the isotropic background component. Galactic source populations, e.g., pulsars, pulsar-wind nebulae, and supernova remnants, however, are concentrated at low latitudes, and undetected members of these populations would be expected to contribute primarily to the Galactic diffuse emission. A population synthesis study presented in Acero et al. (2015) developed a simple model for the spatial, spectral, and luminosity distribution of Galactic γ-ray sources based on the properties of detected Galactic sources. These unresolved sources were estimated to contribute at the level of 3%. For the new IEM we implemented a template for this component using the population synthesis model to draw many sources at random and a calculation of the detection sensitivity of the LAT for the 8-year data set (based on the method described in Abdo et al. 2010) to select members that would not be detected individually.

Figure 3 shows one plane of the model intensity cube for the unresolved Galactic source component. The spatial distribution reflects both the underlying model for luminosity function and distribution of unresolved sources in the Milky Way as well as the variation of the detection sensitivity of the LAT with brightness of the Galactic interstellar emission. Because the interstellar emission is particularly bright at low latitudes, this latter consideration strongly influences the latitude extent of the model unresolved component.

Not surprisingly, the resulting template has large covariance with other diffuse components in the inner Milky Way. Because it represents a known if sub-dominant contribution to the diffuse emission, we retained it in the model as a fixed template.

As the LAT survey deepens, the brighter contributors to the unresolved source component will of course be detected. The luminosity function is fairly steep, and most of the intensity in the unresolved source model is in the faintest sources, i.e., those that will not be resolved from the Galactic interstellar emission.

3.7. *Isotropic diffuse emission*

Integrated over energy, the isotropic diffuse emission represents approximately 25% of the γ-ray intensity of the sky. We adjust it in the first step of the model fitting (High Latitude; see § 4), with independent scale factors at 15 energies between 30 MeV and 1 TeV, where it contributes the greatest fraction of the emission, and hold it fixed through the rest of the fitting sequence. The resulting isotropic component is not strictly a measure of the extragalactic isotropic γ-ray emission because it includes residual charged particle background (LAT triggers misclassified as γ rays). This residual component depends on the event class, event types, and zenith angle limits of the data

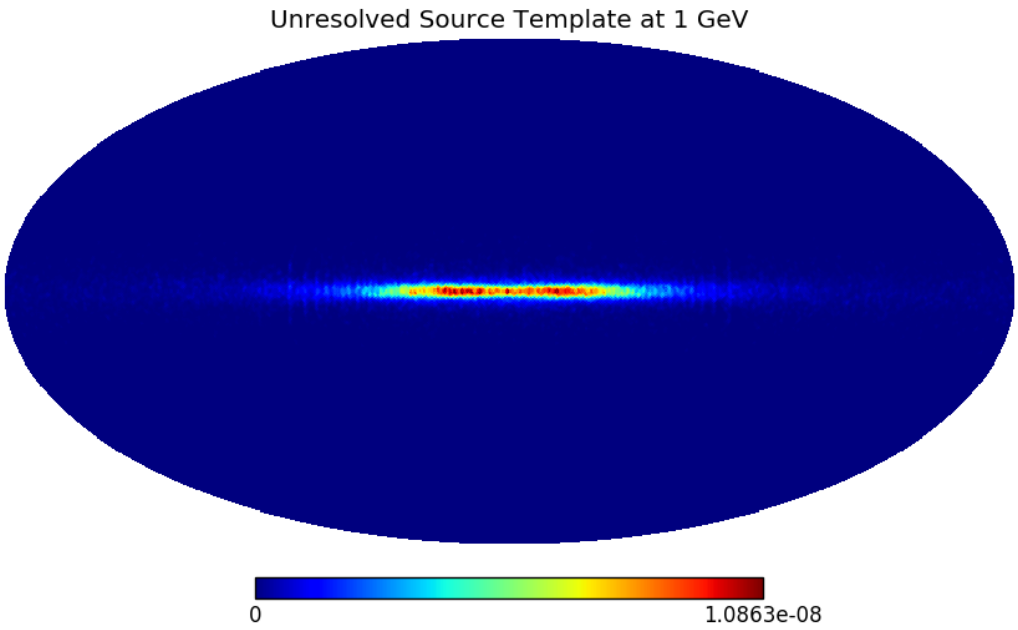

Figure 3. Template adopted to represent the contribution of unresolved Galactic sources; see text for discussion. The image shown is for 1 GeV, and is in Galactic coordinates in Mollweide projection. The scaling is linear and the units of the intensity are $\mathrm{cm}^{-2}\ \mathrm{s}^{-1}\ \mathrm{sr}^{-1}\ \mathrm{MeV}^{-1}$.

selection, and so the isotropic spectrum that results from our model fitting analysis is peculiar to the particular set of selections we have made.

For general use, we have derived isotropic spectra for different event classes and event type selections as a post-processing step, using the Galactic IEM and the 4FGL sources as a fixed foreground. With the release of the Galactic IEM we are providing isotropic template files (FileSpectrum type in the LAT ScienceTools, now Fermitools[5]) for several event classes and event types.

3.8. *Solar & Lunar emission*

The Sun and Moon are effectively diffuse sources of γ rays when considered in long, integrated data sets, as we do for fitting the IEM. The Sun moves through the ecliptic annually, and the Moon completes an orbit of Earth every $\sim$28 days with an orbital plane slightly inclined relative to the ecliptic; the Moon also has significant orbital parallax at the orbit of *Fermi*.

The Moon and the (quiescent) Sun and are passive sources of high-energy γ rays, the Moon from CR interactions in the outer lunar regolith (Moskalenko & Porter 2008) and the Sun from CR interactions in the outer solar atmosphere, and from CR electron IC scattering in the solar radiation field (Abdo et al. 2011; Ackermann et al. 2016). We used the recent lunar γ-ray spectrum of Ackermann et al. (2016) and preliminary updated solar disk and IC spatial/spectra profiles from an analysis of 8 years of LAT data using P8R3 data selections. To make the templates used in the model fitting we used the solar system tools in the LAT ScienceTools/Fermitools[6]. We note in particular that the integrated emission for the Sun and Moon depends on the data selection – time range, zenith angle limit, and

[5] https://fermi.gsfc.nasa.gov/ssc/data/analysis/
[6] https://fermi.gsfc.nasa.gov/ssc/data/analysis/scitools/solar_template.html

maximum rocking angle – because these selections affect the exposure. So separate Solar and Lunar templates were generated for each of the four data selections used in the fit (see § 2). As reported in the cited references, the spectra of the Sun and Moon vary somewhat over the solar cycle; we treat the published spectra as representing time averages for the 8-year time interval that we analyze.

In the model fitting (see § 4) we allowed the solar disk component and the solar IC component to have separate scaling, although the spectral shapes were held fixed in the fits.

4. FITTING PROCEDURE

Our objective is to define a model $I(l, b, E)$ for the physical intensity of the Galactic interstellar emission. We use a maximum likelihood approach, implemented in the Gardian fitting tool (see App. A of Ackermann et al. 2012), to forward-fold the model into data space (predicted counts in spatial and energy bins) and to optimize the free parameters. The emission templates and data are considered in HEALPix binning with pixel size dependent on energy as defined in Table 1, and are processed into 'cubes' of nominal γ-ray intensity maps as a function of energy using a GALPROP model of CR densities. (See § 3.3 for the GALPROP ID, i.e., the GALDEF file designator, of the model; more details about the fitting with Gardian are below.) Figure 4 illustrates the complete set of templates used in the sequence of fits.

In Gardian, the free parameters are scaling factors or functions of energy for the templates mentioned above. Depending on the importance of the template and the nature of the residuals, we use different functions: overall scale factors, power-law functions of energy, or multiply-broken power laws (linear in the logarithm of energy, with either 4 or 8 breaks at energies uniformly spaced in the logarithm).

4.1. *Fitting sequence*

Formally, the analysis in Gardian is a joint optimization over dozens of degrees of freedom. Because different components of the model make their primary contributions in different regions of the sky, we fit the model to the observations in a sequence of regions:

1. High Latitude: $|b| \geq 30°$, excluding the patch region (Section 3.4);
2. Outer Galaxy: $|l - 180°| \leq 90°, |b| \leq 30°$;
3. Inner Galaxy: $|l| \leq 90°$

The regions defined above are illustrated in Figure 5.

In the High Latitude fit, we free the scaling of the local ring (6) atomic hydrogen (denoted HI_6), CO (CO_6), and inverse Compton (IC_6), along with IC_7 and IC_8 in the outer Galaxy (which contribute at high latitudes) and the isotropic spectrum. The IC_9, DNMp, and DNMn components contribute relatively little at high latitudes and were held fixed. We also held fixed the scaling of the patch component (§ 3.4) after some iteration of the fitting sequence. The scaling of the FixedSources template is left free, with a multiply-broken power-law function.

After the High Latitude fit we fit the Outer Galaxy region, freezing the components that had been freed in the first stage. The only exception is the FixedSources template, which is left free. For the Outer Galaxy fit we free the scaling of the DNMp, DNMn, HI_7, HI_8, HI_9, CO_7, and CO_8 rings. The CO_9 ring contains no significant CO emission and we omit it from the fit.

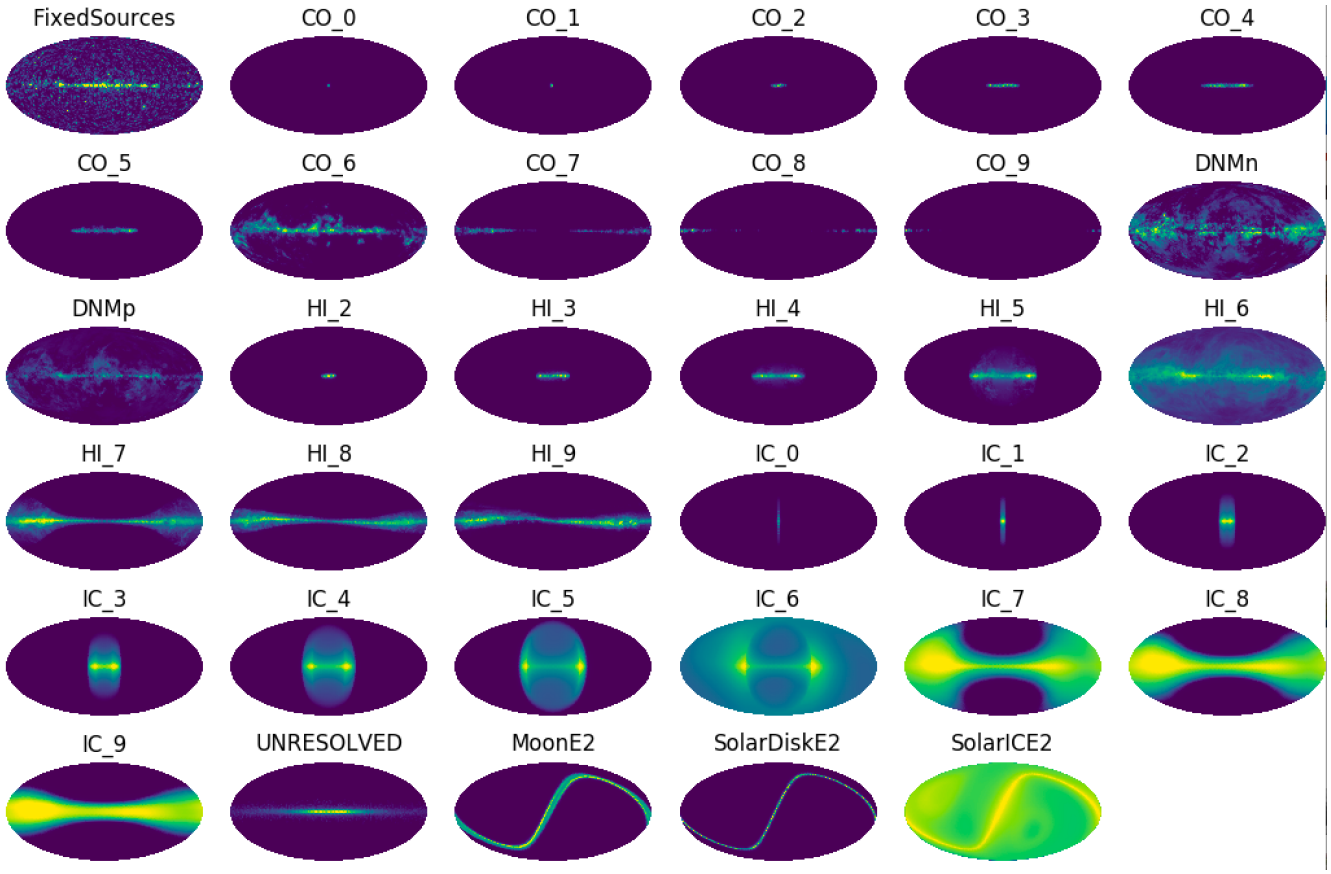

Figure 4. Composite of the set of templates used in the fitting. The images are all-sky maps in Galactic coordinates in Mollweide projection and are predicted counts maps for a single energy range. *The images are independently scaled.* The headings indicate the name of the template, with the numbers indicating the ring (Table 2). Note that no HI_0 or HI_1 ring is defined; this reflects the deficit of atomic gas in the 'Central Molecular Zone'. Also, as discussed in § 3.2, the DNM component is represented by positive (DNMp) and negative (DNMn) contributions. The template for the isotropic component in the fit is not shown.

After the Outer Galaxy fit we fit the Inner Galaxy region, with the free components for the Outer Galaxy fit held fixed, except for the FixedSources template. We free the HI_2, HI_3, HI_4, HI_5, CO_0, CO_1, CO_2, CO_2, CO_4, CO_5, IC_0, IC_1, IC_2, IC_3, IC_4, and IC_5 rings. This fitting sequence hastens convergence in the large-dimensional space of parameters and also helps ensure that the model, while formally maximizing the likelihood function, is also a good representation of regions with wide ranges of γ-ray intensity. The sequence was iterated a number of times, as degrees of freedom in the scaling function were adjusted and as the patch component became successively better defined.

4.2. *Fitting in Gardian*

As mentioned above, the model fitting in Gardian maximizes the Poisson likelihood of the data given the model, with the adjustable parameters being scaling functions (analytical or piecewise continuous) applied to templates of nominally predicted counts (binned spatially and spectrally). As for the 4FGL catalog analysis, we consider LAT data in four energy ranges with different zenith

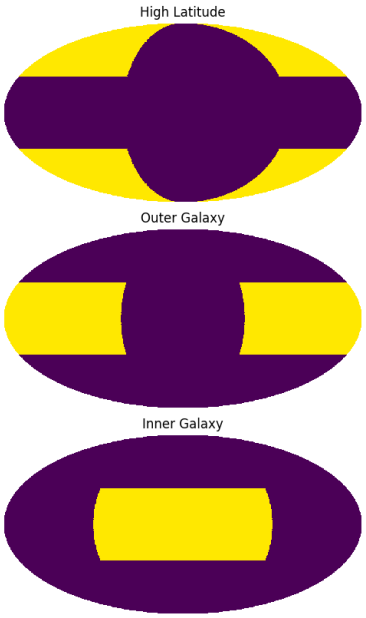

Figure 5. The regions of interest (yellow) used for the sequence of fits in optimizing the parameters of the IEM, in Mollweide projection; see text for the definitions of the regions.

angle limits and PSF event type selections for the different ranges (to construct a data set that is essentially free of residual Earth limb emission).

For the CO and H I rings, predicted counts are calculated in two steps. In the first step, the ring maps are processed in GALPROP according to a model for the distribution of cosmic rays (see § 3.3 for the model specification) along with GALPROP's internal model for the distribution of gas in Galactocentric distance and distance from the plane. GALPROP uses this model as well as an internal model for the Galactocentric distance dependence of $X_{\rm CO} = N({\rm H}_2/W_{\rm CO})$, together with the Galactocentric radius range of a ring, to calculate the effective γ-ray emissivity of the interstellar gas along each line of sight. This is used to construct a spatial-spectral 'cube' of predicted intensity. In the second step, these 'cubes' are multiplied in Gardian by the corresponding exposure cubes and then convolved with an effective point-spread function (PSF). The latter is derived for a direction on the sky that is representative of the overall average; variations of the effective PSF across the sky are mild, but adoption of a uniform PSF is an approximation. The effective PSF is derived from the instrument response functions, taking into account the energy and angle dependence of the angular resolution and energy resolution. Finally, the models are convolved in energy with the energy dispersion function. Like with the PSF, a single effective energy dispersion function is applied over the entire sky. The final IEM can therefore be considered measured in true energies rather than observed energies. Analysis using it will need to apply energy dispersion correction for accurate results.

The scaling functions described above are applied in the fitting (to maximize the likelihood function). This involves another mild approximation that the result of scaling predicted counts maps is effectively the same as scaling the GALPROP-derived templates before multiplication by exposure and convolution.

5. THE MODEL

5.1. *Comparison with the 4-year model*

The 4-year Galactic IEM, `gll_iem_v05.fits`, was developed for Pass 7 Source class and later rescaled for Pass 8 Source as `gll_iem_v06.fits`. In § 5 we described the various new templates. Much of the structure of the Galactic interstellar emission relates to structure in gas of the interstellar medium. This is apparent in Fig. 6, where the improved angular resolution of the gas tracers in the new model is evident.

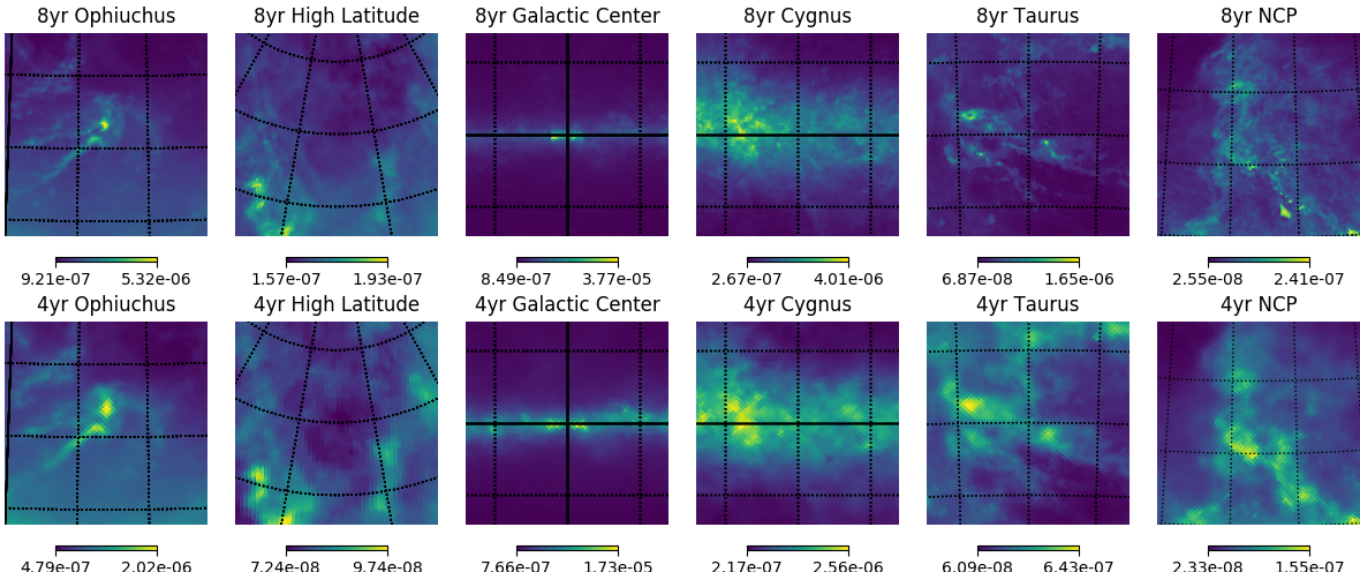

Figure 6. Comparison between 4-year (`gll_iem_v06.fits`) and 8-year (`gll_iem_v07.fits`) models for several 15×15° fields. The images are linearly scaled. The new model has higher resolution and correspondingly greater contrast. The images are for 530 MeV and the units are intensity in $\mathrm{cm}^{-2}\ \mathrm{s}^{-1}\ \mathrm{sr}^{-1}\ \mathrm{MeV}^{-1}$. From left to right, the field centers in Galactic coordinates are (353°, 16°), (90°, 75°), (0°, 0°), (75°, 0°), (170°, −15°), (123°, 27°). The latter is the northern celestial pole.

The new model was considered adequate for the production of the catalog, and quantitatively represents an overall improvement relative to the 4-year model in terms of representation of the sky when the source component is also considered.

5.2. *Caveats*

In the production of the 4FGL catalog we recognized some shortcomings in the new Galactic IEM. These issues were not considered serious for the production of the catalog; their influence was in effect mitigated in the catalog analysis process, which subdivided the sky into hundreds of regions analyzed individually, and gave the diffuse emission model two spectral degrees of freedom (power-law index and normalization) in each region. Below we provide brief descriptions of the issues. We anticipate releasing an updated 8-year IEM when they are addressed. **In any case, the `gll_iem_v07.fits` model is not recommended for study of medium or large-scale structures in the high-energy sky.**

- Structure introduced in the gas rings by processing into Gardian templates. The structure introduced in the gas rings in generating templates for the Gardian fitting (see § 4.2) included some features related to mismatching of the GALPROP-internal model for gas distribution and the distribution implied using the rotation curve that was used to generate the gas rings. This introduced some low-contrast modulation of the rings, particularly at low latitudes.

- Brightness/spectrum/smoothness of the patch component. The patch component is derived as a 'non-template' component determined by residuals from an (iterative) fit of the all-sky data (§ 3.4), with part of the procedure being fitting the residuals with a doubly-broken power-law spectral model (consistent with what could represent inverse-Compton emission from different populations of CR electrons), and then defining the patch template from spatially smoothing the fit parameters (normalizations and spectral indices). The spectral model is not perfect, of course, and the power-law approximation over-predicts the patch emission at energies well below the lower-energy break (150 MeV) and well above the higher-energy break (3 GeV). At the highest energies, because only positive residuals were considered in fitting the model, the spectrum is somewhat biased (too hard) and the component has low-level structure from positive fluctuations of the residuals. This is primarily a cosmetic effect but could be avoided.

- DNM and gas template consistency. For technical reasons, the DNM positive and negative maps were not processed through GALPROP to make templates for Gardian fitting but instead were defined with an emissivity spectrum that was independent of direction. This is not a bad approximation but as a Gardian template, effectively the DNM component no longer strictly represents a component of the dust optical depth that is not correlated with either the CO or H I emission.

- Roughness of the unresolved Galactic source template. The unresolved source template (§ 3.6), which was generated with Monte Carlo sampling of sources drawn from a luminosity function and a spatial distribution model, is made up of many simulated faint sources. Each individual source is modeled with a power-law spectrum, and although the unresolved Galactic source template is relatively faint in general, at the lowest energies, the individual sources with the softest spectra can become relatively bright, making the template unrealistically lumpy.

- Systematic uncertainty in the instrument response functions. The P8R3 IRFs used for evaluating exposures and predicted counts are not entirely consistent between the PSF event types. This affects the accuracy of the effective PSF used in the Gardian fitting. The effects are not dramatic but a correction to the IRFs based on flight data is being evaluated for eventual release.

The *Fermi* LAT Collaboration acknowledges generous ongoing support from a number of agencies and institutes that have supported both the development and the operation of the LAT as well as scientific data analysis. These include the National Aeronautics and Space Administration and the Department of Energy in the United States, the Commissariat à l'Energie Atomique and the Centre National de la Recherche Scientifique / Institut National de Physique Nucléaire et de Physique des Particules in France, the Agenzia Spaziale Italiana and the Istituto Nazionale di Fisica Nucleare in Italy, the Ministry of Education, Culture, Sports, Science and Technology (MEXT), High Energy

Accelerator Research Organization (KEK) and Japan Aerospace Exploration Agency (JAXA) in Japan, and the K. A. Wallenberg Foundation, the Swedish Research Council and the Swedish National Space Board in Sweden.

Additional support for science analysis during the operations phase is gratefully acknowledged from the Istituto Nazionale di Astrofisica in Italy and the Centre National d'Études Spatiales in France. This work performed in part under DOE Contract DE-AC02-76SF00515.

Facility: Fermi

Software: Gardian

REFERENCES

Abazajian, K. N., & Kaplinghat, M. 2012, PhRvD, 86, 083511

Abdo, A. A., Ackermann, M., Ajello, M., et al. 2010, ApJS, 188, 405

—. 2011, ApJ, 734, 116

Acero, F., Ackermann, M., Ajello, M., et al. 2015, ApJS, 218, 23

—. 2016, ApJS, 223, 26

Ackermann, M., Ajello, M., Atwood, W. B., et al. 2012, ApJ, 750, 3

Ackermann, M., Ajello, M., Albert, A., et al. 2016, PhRvD, 93, 082001

Clemens, D. P. 1985, ApJ, 295, 422

Górski, K. M., Hivon, E., Banday, A. J., et al. 2005, ApJ, 622, 759

Grenier, I. A., Casandjian, J.-M., & Terrier, R. 2005, Science, 307, 1292

Haslam, C. G. T., Salter, C. J., Stoffel, H., & Wilson, W. E. 1982, A&AS, 47, 1

HI4PI Collaboration, Ben Bekhti, N., Flöer, L., et al. 2016, A&A, 594, A116

Hooper, D., & Goodenough, L. 2011, Physics Letters B, 697, 412

Kalberla, P. M. W., Burton, W. B., Hartmann, D., et al. 2005, A&A, 440, 775

Lebrun, F., Paul, J. A., Bignami, G. F., et al. 1982, A&A, 107, 390

Moskalenko, I. V., & Porter, T. A. 2008, in Lunar and Planetary Inst. Technical Report, Vol. 39, Lunar and Planetary Science Conference, 2300

Planck Collaboration, Aghanim, N., Ashdown, M., et al. 2016, A&A, 596, A109

Porter, T. A., Jóhannesson, G., & Moskalenko, I. V. 2017, ApJ, 846, 67

Porter, T. A., Moskalenko, I. V., Strong, A. W., Orlando, E., & Bouchet, L. 2008, ApJ, 682, 400

Schlegel, D. J., Finkbeiner, D. P., & Davis, M. 1998, ApJ, 500, 525

Sofue, Y. 2015, PASJ, 67, 75

Su, M., Slatyer, T. R., & Finkbeiner, D. P. 2010, ApJ, 724, 1044

Wolleben, M. 2007, ApJ, 664, 349